



Spectroscopically Identified Emission Line Galaxy Pairs in the WISP Survey*

Y. Sophia Dai (戴昱)¹, Matthew M. Malkan², Harry I. Teplitz³, Claudia Scarlata⁴, Anahita Alavi⁵, Hakim Atek⁶, Micaela Bagley⁷, Ivano Baronchelli⁸, Andrew Battisti⁹, Andrew J Bunker^{10,11}, Nimish P. Hathi¹², Alaina Henry¹², Jiasheng Huang¹, Gaoxiang Jin¹, Zijian Li¹, Crystal Martin¹³, Vihang Mehta⁴, John Phillips⁴, Marc Rafelski^{12,14}, Michael Rutkowski¹⁵, Hai Xu¹, Cong K Xu¹, and Anita Zanella¹⁶

¹ Chinese Academy of Sciences South America Center for Astronomy (CASSACA), National Astronomical Observatories of China (NAOC), 20A Datun Road, Beijing, 100012, People's Republic of China; daysophia@gmail.com

² UCLA Department of Physics and Astronomy, Los Angeles, CA 90095-1547, USA

³ IPAC, Mail Code 314-6, Caltech, 1200 East California Blvd., Pasadena, CA 91125, USA

⁴ Institute for Astrophysics, University of Minnesota, 116 Church Street Southeast, Minneapolis, MN 55455, USA

⁵ IPAC, California Institute of Technology, 1200 East California Boulevard, Pasadena, CA 91125, USA

⁶ Sorbonne Université, CNRS UMR 7095, Institut d'Astrophysique de Paris, 98 bis boulevard Arago, F-75014, Paris, France

⁷ College of Natural Sciences, The University of Texas at Austin, 2515 Speedway, Austin, TX 78712, USA

⁸ Dipartimento di Fisica e Astronomia, Università di Padova, vicolo Osservatorio, 3, I-35122 Padova, Italy

⁹ Research School of Astronomy and Astrophysics, Australian National University, Cotter Road, Weston Creek, ACT 2611, Australia

¹⁰ Sub-department of Astrophysics, Department of Physics, University of Oxford, Denys Wilkinson Building, Keble Road, Oxford OX1 3RH, UK

¹¹ Kavli Institute for the Physics and Mathematics of the Universe (WPI), The University of Tokyo Institutes for Advanced Study, The University of Tokyo, Kashiwa, Chiba 277-8583, Japan

¹² Space Telescope Science Institute, 3700 San Martin Drive, Baltimore, MD 21218, USA

¹³ Department of Physics, Broida Hall, University of California Santa Barbara, CA 93106, USA

¹⁴ Department of Physics and Astronomy, Johns Hopkins University, Baltimore, MD 21218, USA

¹⁵ Department of Physics and Astronomy, Minnesota State University-Mankato, Trafton North 141, Mankato, MN, 56001, USA

¹⁶ Istituto Nazionale di Astrofisica, Vicolo dell'Osservatorio 5, I-35122 Padova, Italy

Received 2021 January 11; revised 2021 September 19; accepted 2021 October 11; published 2021 December 20

Abstract

We identify a sample of spectroscopically measured emission line galaxy (ELG) Pairs up to $z = 1.6$ from the Wide Field Camera 3 (WFC3) Infrared Spectroscopic Parallels (WISP) survey. WISP obtained slitless, near-infrared grism spectroscopy along with direct imaging in the J and H bands by observing in the pure-parallel mode with the WFC3 on board the Hubble Space Telescope. From our search of 419 WISP fields covering an area of $\sim 0.5 \text{ deg}^2$, we find 413 ELG pair systems, mostly H_α emitters. We then derive reliable star formation rates (SFRs) based on the attenuation-corrected H_α fluxes. Compared to isolated galaxies, we find an average SFR enhancement of 40%–65%, which is stronger for major Pairs and Pairs with smaller velocity separations ($\Delta_v < 300 \text{ km s}^{-1}$). Based on the stacked spectra from various subsamples, we study the trends of emission line ratios in pairs, and find a general consistency with enhanced lower ionization lines. We study the pair fraction among ELGs, and find a marginally significant increase with redshift $f \propto (1+z)^\alpha$, where the power-law index $\alpha = 0.58 \pm 0.17$ from $z \sim 0.2$ to ~ 1.6 . The fraction of active galactic nuclei is found to be the same in the ELG Pairs as compared to the isolated ELGs.

Unified Astronomy Thesaurus concepts: Galaxy evolution (594); Galaxy pairs (610); Galaxy interactions (600); Extragalactic astronomy (506); Interacting galaxies (802); High-redshift galaxies (734); Galaxy spectroscopy (2171)

Supporting material: machine-readable tables

1. Introduction

Mergers and interactions play a key role in galaxy evolution. In addition to large scale accretion of baryonic and dark matter (e.g., Di Matteo et al. 2008; Dekel et al. 2009; Steidel et al. 2010; Bournaud et al. 2011), galaxy mergers can convert gas into stars, and feed the growth of supermassive black holes (e.g., White & Rees 1978; Mihos & Hernquist 1996; Sanders & Mirabel 1996). Both simulations and observations suggest that

galaxy interactions elevate star formation, especially in the center of the galaxy (e.g., Sanders & Mirabel 1996; Di Matteo et al. 2007; Ellison et al. 2008; Fensch et al. 2017). The degree of star formation rate (SFR) enhancement may depend on galaxy mass ratios, separation of the galaxies, and amount of gas (e.g., Cox et al. 2008; Patton et al. 2013; Davies et al. 2015; Scudder et al. 2015; Moreno et al. 2021). Locally, the SFR enhancement has been confirmed in large statistical samples, with a pair separation up to 150 kpc (Ellison et al. 2013; Patton et al. 2013; Violino et al. 2018), when compared to a control sample of isolated galaxies with similar stellar mass. At higher redshifts, however, the situation is less clear due to limited observations and identifications of pair samples, though controversy exists as to whether mergers are the main driver of star formation and mass assembly since $z \sim 4$ (e.g., de Ravel et al. 2009; Williams et al. 2011; Wuyts et al. 2011; Tasca et al. 2014).

Given its fundamental importance to galaxy assembly and size evolution over cosmic time, many investigators have tried to

* Based on observations made with the NASA/ESA Hubble Space Telescope, which is operated by the Association of Universities for Research in Astronomy, Inc., under NASA contract NAS 5-26555. These observations are associated with programs 11696, 12283, 12568, 12092, 13352, 13517, and 14178.



Original content from this work may be used under the terms of the [Creative Commons Attribution 4.0 licence](https://creativecommons.org/licenses/by/4.0/). Any further distribution of this work must maintain attribution to the author(s) and the title of the work, journal citation and DOI.

measure the galaxy merger rate. Due to the large uncertainties associated with the merging timescale, wide Pairs are often used, assuming they will merge at some point in the future. Observational and theoretical studies have shown that pair fractions, and thus merger rates, depend on mass ratios, luminosities, and optical colors (e.g., Patton & Atfield 2008; Hopkins et al. 2010; Lotz et al. 2011; Keenan et al. 2014; De Propriis et al. 2014; López-Sanjuan et al. 2015). For instance, the major-merger rate appears to evolve as $(1+z)^\alpha$, where $\alpha = 2-3$, as predicted by simulations and confirmed by observations (e.g., Bridge et al. 2010; Xu et al. 2012b; López-Sanjuan et al. 2015; Rodriguez-Gomez et al. 2015; Man et al. 2016; Ventou et al. 2017; Duncan et al. 2019), at least up to a possible peak around $z \sim 3$ (e.g., Conselice & Arnold 2009; Kaviraj et al. 2015; Ventou et al. 2017; Qu et al. 2017; Mantha et al. 2018). Others have found a flatter or close-to-constant merger fraction, especially among massive galaxies ($\log M_* > 10.3 M_\odot$), as in Duncan et al. 2019 ($\alpha = 0.8 \pm 0.2$, $z = 0.5-6$) and in Williams et al. 2011 ($\alpha = -0.4 \pm 0.6$, $z = 0.4-2$). These observational differences can be attributed to different selection effects and the different conversion factors between pair fraction and merger rate (Mantha et al. 2018; Duncan et al. 2019). For instance, after converting the observed pair fraction to merger rate, a constant merger rate was found up to $z \sim 3$ in simulations (Snyder et al. 2017), and to $z \sim 6$ in observations (Duncan et al. 2019). At higher redshifts ($z > 3$), a steady decrease is noticed by both simulations up to $z \sim 4$ (e.g., Snyder et al. 2017) and observations up to $z \sim 6$ (e.g., Ventou et al. 2017). In general, up to $z \sim 2.5$, pair fractions are found to be 2%–16% for major mergers (mass ratio < 4), and $\sim 20\%$ – 30% if minor mergers (mass ratio > 4) are included (e.g., Ellison et al. 2008; Keenan et al. 2014; Man et al. 2016; Mantha et al. 2018; Zanella et al. 2019).

The uncertainties in the merger rate measurement at $z \geq 1$ are caused by various factors, including sample selection, pair morphology, and merging timescales (e.g., Law et al. 2015; López-Sanjuan et al. 2015; Snyder et al. 2017; Mantha et al. 2018; Duncan et al. 2019). At $z > 0.5$, pair identification becomes more difficult, mostly related to the increasing uncertainties in photometric redshifts and declining resolution for morphology identifications. High spatial resolution imaging and accurate redshift information, preferably spectroscopic z , are desired. False pair identification is high ($> 50\%$) from morphological identification alone, due to chance sky alignments (e.g., Patton & Atfield 2008; Chou et al. 2012; Law et al. 2012, 2015). Ground-based spectroscopy is only available for small samples (e.g., Law et al. 2015), or limited to local galaxies ($z < 0.2$), as large separations are required for multi-object spectrographs (e.g., Ellison et al. 2008). For instance, Sloan Digital Sky Survey (SDSS) Pairs are biased to large separation ($> 55''$) systems to avoid slit/fiber collisions. Xu et al. (2012b) studied the merger rates of close major-merger Pairs using a K -band selected local ($z \sim 0$) sample and a sample of $0.2 \leq z \leq 1$ Pairs selected using high quality photo z data in the Cosmic Evolution Survey (COSMOS) field, both having high completeness and reliability. On the other hand, the $z > 1$ studies, mostly based on estimates for massive and luminous galaxies (e.g., Bundy et al. 2009; Bridge et al. 2010; Williams et al. 2011), usually have large uncertainties due to small sample sizes and incomplete spectroscopic redshifts (e.g., Bluck et al. 2012). Compared to major mergers selected by stellar mass ratios, those selected by optical flux ratios show a

systematically higher and increasing merger fraction (Lotz et al. 2011; Man et al. 2016; Mantha et al. 2018).

Earlier studies of spectroscopically identified $z > 1$ pairs, though limited, have found generally consistent properties with statistical, photometric samples. In a study of 113 spectroscopic Pairs from the deep Multi Unit Spectroscopic Explorer observations in the Hubble Ultra Deep Field, Ventou et al. (2017) show that the fraction of Pairs increases up to $z \sim 3$ and then slowly decreases. The star formation conditions, however, seem to diverge in different spectroscopic pair samples. At $z < 1$, Wong et al. (2011) found that tidal interactions are responsible for a 15%–20% increase of specific SFR ($sSFR = SFR/M_*$) in pairs, as compared to isolated galaxies. In this study based on the Prism Multi-Object Survey, no significant redshift dependence was found. At $z > 2$, however, a small number (two) of spectroscopically confirmed Pairs show similar star-forming properties as $z \sim 2$ main-sequence galaxies (Law et al. 2015). Based on 30 spectroscopic Pairs from the MOSFIRE Deep Evolution Field Survey (Kriek et al. 2015), Wilson et al. (2019a) also found no measurable SFR enhancement or metallicity deficit for $1.4 < z < 3.8$ Pairs as compared to isolated galaxies with similar stellar masses. This can be explained by the earlier merger stages (e.g., pre-coalescence) before the triggering of starburst (Bustamante et al. 2018).

To reconcile the uncertainties associated with photometric redshifts and declining resolution for morphology identifications at $z > 0.5$, a statistically significant sample of spectroscopically confirmed galaxy Pairs is needed. In this paper, we search for galaxy Pairs using the high spatial resolution spectra in the Hubble Space Telescope’s (HST) Wide Field Camera 3 (WFC3) Infrared Spectroscopic Parallel survey (WISP; PI: M. Malkan, GO# 11696, 12283, 12568, 12902, 13352, 13517, 14178) (Atek et al. 2010), which includes ~ 9000 high signal-to-noise (S/N) ratio emission line galaxies (ELGs) with spectroscopic redshifts. WISP is a Hubble Space Telescope pure-parallel survey, which observes *random* parallel fields with the WFC3, obtaining direct imaging (IR, and sometimes UVIS) and IR grism spectroscopy ($0.8-1.7 \mu\text{m}$) simultaneously. WISP detects ELGs without preselection, allowing one of the first spectroscopic studies of faint, possibly low-mass, sometimes low-metallicity ELG Pairs up to $z = 1.5$. Many of the WISP-discovered strong ELGs, with their high equivalent width (EW), are the local analogs of the sources of re-ionization at $z > 6$ (Atek et al. 2014).

We introduce the ELG pair sample in Section 2, then study their star formation properties in Section 3. In Section 4, we stack the pair spectra in different bins and study their emission line ratios, followed by analysis of the pair fraction and AGN fraction in Section 5, before a brief summary (Section 6). Throughout, we assume a Λ -dominated flat universe, with $H_0 = 70 \text{ km s}^{-1} \text{ Mpc}^{-1}$, $\Omega_\Lambda = 0.7$, $\Omega_M = 0.3$. All magnitudes are in the AB system.

2. The ELG Pair Sample

2.1. The WISP Survey

The sample of ELG Pairs was selected from the WISP survey. WISP obtained slitless, near-infrared grism spectroscopy along with direct imaging in the J and H bands, by observing in the pure-parallel mode with the WFC3 on board HST over ~ 1000 orbits.¹⁷ The spectra are obtained with the

¹⁷ <https://archive.stsci.edu/prepds/wisp/>

G102 ($\lambda = 0.8\text{--}1.15\ \mu\text{m}$, $R \sim 210$) and G141 grisms ($\lambda = 1.075\text{--}1.70\ \mu\text{m}$, $R \sim 130$), together with direct imaging in the J and I or H bands (F110W and F140W/F160W, respectively). Out of the 483 fields observed, F140W is used in 190 fields and F160W in 289 fields.¹⁸ For convenience, hereafter the H band is referred to either as the F140W or F160W band, depending on the actual filter used. For some fields, WFC3/UVIS imaging in the F606W and F814W bands are also available. The WFC3 data were reduced through a customized pipeline updated from Atek et al. (2010). Each field was examined by at least two reviewers via a customized interface for redshift identification.

Each WISP field of view covers a projected area of $2\frac{1}{3} \times 2\frac{1}{2}$, corresponding to $\sim 350\ \text{kpc}^2$ at $z = 1\text{--}2$. The WISP HST/WFC3 imaging data have a pixel scale of $0''.13\ \text{pix}^{-1}$. The spectroscopic redshift was measured from the emission lines detected in the G102 and the G141 grisms. A typical ELG flux limit in WISP for an H_α emission line ($H_{\alpha,\text{raw}}$, [N II] not corrected) is $\sim 5 \times 10^{-17}\ \text{erg s}^{-1}$ (5σ). More details regarding the line identification are given in Section 2.3.

2.2. The Pair Sample

We calculated the angular separations based on the sky positions, and then the projected physical separation D_{proj} (in $h^{-1}\ \text{kpc}$) using the average z of the members. The comoving velocity offset Δ_V (in kpc s^{-1}) was calculated from the redshifts of the pair members. All ELG Pairs have at least an H_α (6564 Å, [N II] corrected) or [O III] (5007 Å, 4959 Å) line detected at $S/N > 3$. The Pairs are further divided into three groups based on their physical separations and velocity differences (see also Figure 1):

1. Merging Pairs ($2 < D_{\text{proj}} < 5\ h^{-1}\ \text{kpc}$, $\Delta_V < 500\ \text{km s}^{-1}$),
2. Secure Pairs ($5 < D_{\text{proj}} < 50\ h^{-1}\ \text{kpc}$, $\Delta_V < 500\ \text{km s}^{-1}$),
3. Wide Pairs ($D_{\text{proj}} < 105\ h^{-1}\ \text{kpc}$, $\Delta_V < 1000\ \text{km s}^{-1}$).¹⁹

Pairs that are < 2 pixels apart, corresponding to a D_{proj} of $\sim 2\ \text{kpc}$ at $z = 1.5$, are not resolvable with HST's spatial resolution. In this pair sample, the angular separation ranges from $0''.28\text{--}30''.6$, with a median of $10''.3$. Most of our pair sample consists of compact members, while 112 systems ($27\% \pm 3\%$) are identified as disturbed systems, showing evidence of tidal tails or disturbed morphology based on visual inspections.

A total of 413 spectroscopically identified ELG pair systems are selected from a parent sample of 8192 ELGs in 419 WISP fields. The pair sample consists of 24 merging pairs, 108 secure pairs, and 281 wide pairs. For a fraction (108/413, $\sim 26\%$) of the WISP pairs, Spitzer Infrared Array Camera (IRAC) observations are also available (PI: Colbert, ID: 80134, 90230, 10041, 12093). For these objects we gathered multi-wavelength data from HST (UVIS, J , H), ground-based photometry follow-up with the Palomar 5.0 m, Magellan 6.5 m, or WIYN 3.5 m telescopes (in the u , g , r , i bands), to the IRAC (3.6 and $4.5\ \mu\text{m}$) bands (A. Battisti et al. 2021, in preparation; I. Baronchelli et al. 2021, in preparation). The stellar mass was then estimated using the Cod Investigating GALaxy Emission (CIGALE) spectral energy distribution (SED)-fitting code (Noll et al. 2009; Boquien et al. 2019),

¹⁸ Another four fields were observed in F110W only but not used in this work.

¹⁹ $105\ h^{-1}\ \text{kpc}$ was chosen as an equivalent of $150\ \text{kpc}$ for $h = 0.7$. This value is chosen as the separation upper limit where SFR enhancement has been previously reported in Pairs in the literature (e.g., in local SDSS galaxy pairs; Patton et al. 2013).

assuming a Chabrier IMF, an exponential star formation history in steps of 0.1 dex, variable metallicity between 0.004 and 0.05, and the Charlot & Fall (2000) dust attenuation law.

Tables 1 and 2 summarized the basic properties of the pair sample. The full Pairs catalogs are provided in the online version of the paper. Figure 1 shows the distribution of D_{proj} and Δ_V of the pair sample. The pair sample does not peak at any specific projected separations or velocity offset, except for merging pairs, which gather at the smallest velocity and physical separations.

2.2.1. Major Pair Fraction

For the subsample of 108 Pairs with stellar mass estimates, 47/108 (44%) can be classified as major mergers (mass ratio $< 4:1$) and 61/108 (56%) as minor mergers (mass ratio $> 4:1$). In comparison, the major-merger fraction based on the H -band flux ratio for the full sample of 413 Pairs is systematically higher, at $\sim 69\%$ for major (H -band flux ratio $< 4:1$) and $\sim 31\%$ for minor (H -band flux ratio $> 4:1$) pairs, respectively. This is consistent with what was found previously in the UltraVISTA/COSMOS pairs, in which the fraction of H -band selected major Pairs are higher than stellar mass-selected major Pairs (Man et al. 2016).

2.2.2. Higher-order Systems

Among the 413 ELG pairs, there are also 47 multiple systems, including 36 triplets, four quadruple systems, and seven quintuple systems. This fraction of $\sim 11\% \pm 2\%$ of higher-order systems is significantly higher than the $\sim 5\%$ reported in SDSS galaxy Pairs (Ellison et al. 2008). By design, SDSS and WISP are targeting different samples with different selections, namely a multiparameter color selection in SDSS versus WISP's emission line selection. In addition, SDSS adopted a much more complicated pair sample selection (10 criteria) than in this WISP sample (three criteria). Both can contribute to this significant difference. Our fraction is otherwise close to the result for ELGs in Zanella et al. (2019), who found that 13% of their ELGs have multiple *satellites*. In the following analyses, the multiple systems are counted as one *pair*, similar to the SDSS approach (Ellison et al. 2008), and the properties of the brightest pair members are used except otherwise noted.

2.3. The Control Sample

A control sample of 4070 ELGs was then selected from the isolated ELGs to have the same redshift distribution as the pair sample, also requiring at least an H_α ([N II] corrected, see Section 2.4) or [O III] emission line flux detected with $S/N > 3$. The selection was done by choosing 10 isolated galaxies for each ELG pair system in the same redshift bin of the primary member, with a bin size of 0.1, with no duplications. If fewer than 10 galaxies are available, we just use those. The redshift distributions of the control and pair samples are required to be identical by design, as confirmed by Kolmogorov–Smirnov (K-S) test probabilities of $p = 0.79, 0.96$, and 0.96 that there are no differences, for the combined z distribution, and the individual z distribution for the primary and secondary pair members, respectively. Figure 2 (top) shows the redshift distribution ELG pair sample (413), the control sample of isolated ELGs (4070), and the parent ELG sample (8192).

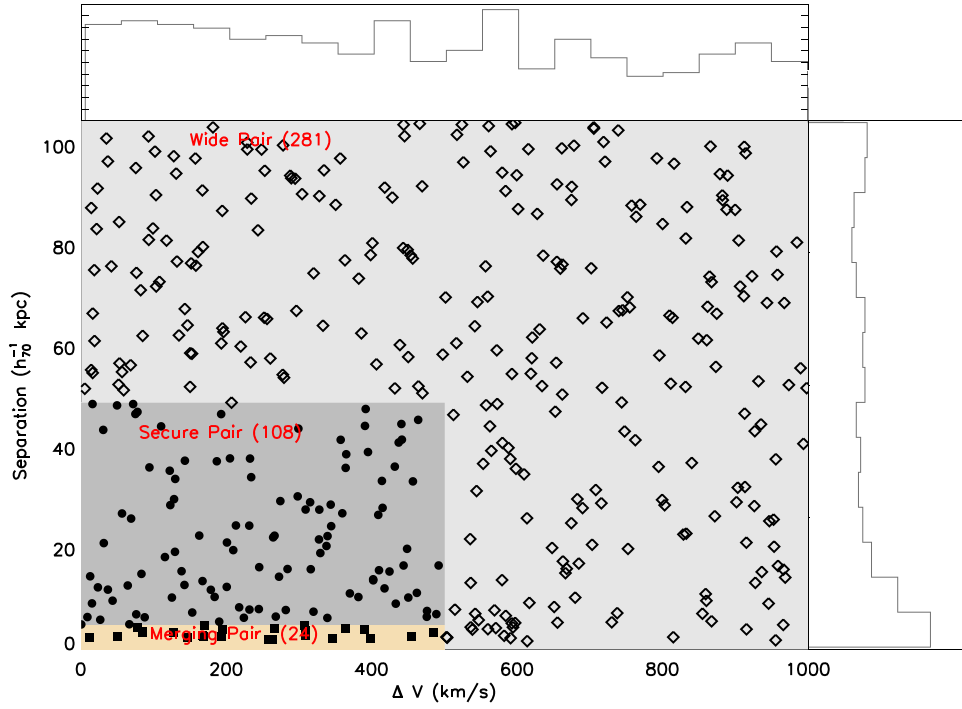


Figure 1. Distribution of ELG Pairs in the projected separation and relative velocity space. Histograms in the top and side panels show the distribution in the two axes. A total of 413 ELG pair systems are identified, including 24 merging (filled squares), 108 secure (filled circles), and 281 wide Pairs (open diamonds; for definition, see Section 2). Systems with >2 members are plotted only once, represented by the closest Pairs of the group. The WFC3 resolution is $0''.13 \text{ pixel}^{-1}$, while a minimum of 2 pixels is required to spatially resolve the galaxies. At redshift ~ 1 , this corresponds to a resolution of $\sim 1 \text{ kpc}$.

Table 1
ELG Pair Sample

WISPID	R.A.(p)	Decl.(p)	R.A.(s)	Decl.(s)	Sep ($h_{70}^{-1} \text{ kpc}$)	Δ_V (km s^{-1})
1-10_1-195	16.671364	15.151823	16.671064	15.1524	9.28	616.4
1-28_1-124	16.634722	15.147898	16.634201	15.148602	16.03	667.8
5-41_5-67	216.785309	57.852722	216.784805	57.850578	46.60	512.0

Note. R.A. and decl. are in J2000; “p” in the bracket denotes the primary galaxy, “s” for the secondary galaxy. The typical redshift uncertainty is $\sim 0.1\%$ (Colbert et al. 2013), which translates to a velocity uncertainty of $\sim 70\text{--}200 \text{ km s}^{-1}$, depending on the actual redshift of the pair members. The full catalog is available in the online version of the paper.

(This table is available in its entirety in machine-readable form.)

Table 2
Galaxy Properties of the ELG Pair Sample

WISPID	$z(p)$	$z(s)$	Hflag	$H(p)$ (AB)	$H(s)$ (AB)	$H_{\alpha}(p)$ $10^{-17} \text{ erg s}^{-1}$	$H_{\alpha}(s)$ $10^{-17} \text{ erg s}^{-1}$	$SFR(p)$ ($M_{\odot} \text{ yr}^{-1}$)	$SFR(s)$ ($M_{\odot} \text{ yr}^{-1}$)
1-10_1-195	0.5084	0.5057	1	20.5	24.5	16.6 ± 3.4	5.1 ± 1.5	2.2 ± 0.4	0.5 ± 0.1
1-28_1-124	1.3444	1.3396	1	22.2	24.0	13.1 ± 3.6	4.4 ± 1.7	19.1 ± 5.3	4.5 ± 1.7
5-41_5-67	1.3444	1.3481	1	21.9	22.3	17.6 ± 1.3	7.2 ± 1.8	25.6 ± 1.9	10.6 ± 2.6

Note. “p” in the bracket denotes the primary galaxy, “s” for the secondary galaxy. Hflag: “0” for the default F160 filter, “1” for the F140 filter. The typical redshift uncertainty is $\sim 0.1\%$ (Colbert et al. 2013), which translates to a velocity uncertainty of $\sim 70\text{--}200 \text{ km s}^{-1}$, depending on the actual redshift. Here, H_{α} refers to the [N II]-corrected H_{α} flux (see Section 2.4). SFRs are based on the [N II]-removed H_{α} flux, and corrected for dust extinction (see Section 3). The full catalog is available in the online version of the paper.

(This table is available in its entirety in machine-readable form.)

The pair and control samples show a generally comparable redshift distribution, with two broad peaks around $z = 0.5$ and $z = 1.1$, corresponding to the redshifts at which H_{α} falls in the most sensitive wavelength range of the grism coverages

(throughput $>10\%$, G102: $0.81\text{--}1.15 \mu\text{m}$, G141: $1.08\text{--}1.69 \mu\text{m}$). Compared to the parent ELG sample, Pairs are less often found at $z > 1.5$ and $0.7 < z < 0.9$, due to the S/N requirement for both pair members. The reasons are twofold. First, at the

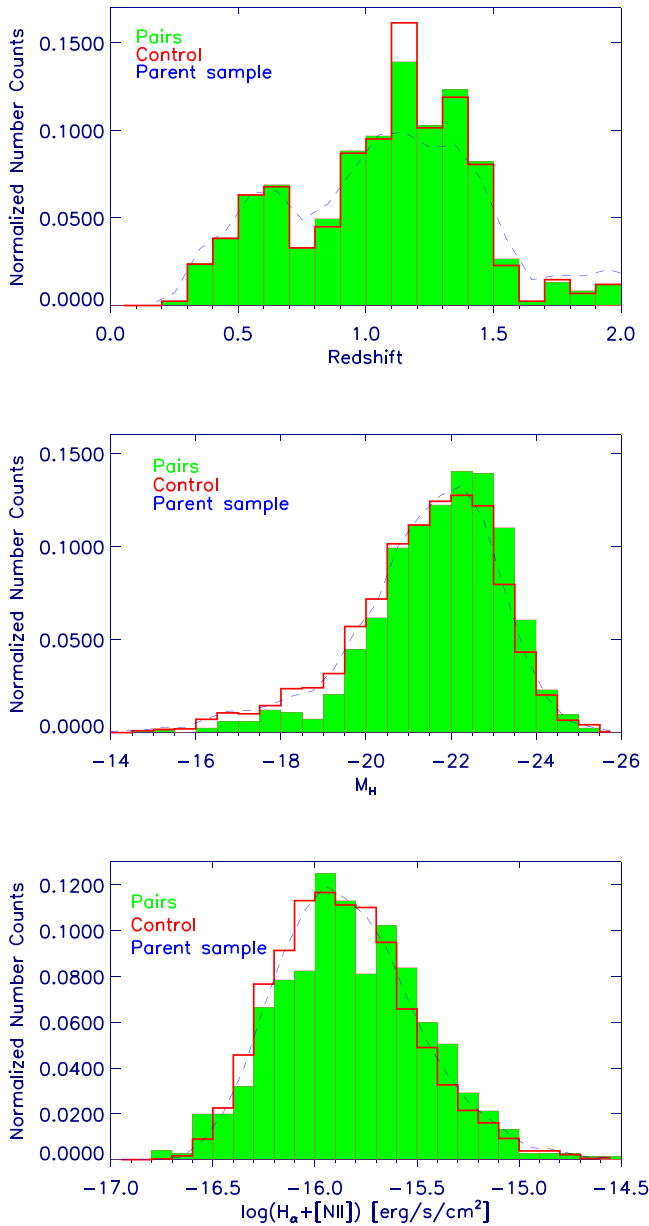


Figure 2. Redshift (top), absolute H -band magnitude (K corrected, middle), and raw H_α flux (bottom) distributions of the ELG Pairs (solid green), the control sample of isolated ELGs (red), and the parent ELG sample (blue dashed line). The increasing difficulties of line identification explain the steep drop at $z > 1.5$, where the H_α line falls out of the wavelength coverage, while the lower S/N at the G102/G141 overlapped region and misidentification of single-line emitters contribute to the drop at $z = 0.8$ – 1.1 . The K-S test of the similarity between the pair and control sample for the redshift, M_H , and H_α gives probabilities of 0.79, 0.005, and $< 1e-4$, respectively.

intermediate redshifts of $0.7 < z < 0.9$, where the two grisms overlap, the spectra are typically noisier due to the reduced sensitivities in the overlap regions. This increases the chances of missed emission lines and misidentifications. Given the requirement of line detection in both ELGs to make place them in the pair sample, the ELG incompleteness is doubled for pairs, which contributes to the deeper drop in number distribution at $0.7 < z < 0.9$.

In addition, at $z > 1.5$, as H_α shifts beyond the red limit of the G141 grism coverage, the redshifts are identified by [O III] emission lines. Based on observations up to $z = 1.5$, for the same object, [O III] lines are generally weaker than the H_α

emissions, and thus more difficult to detect (Mehta et al. 2015). In fact, only 7% of our pair sample are [O III]-only pairs. According to simulation results, in the case of a single emission line, about 6% of the H_α lines could be misidentified as [O III] lines (Colbert et al. 2013). On the other hand, single-line [O III] emitters are rare, as they are often show a marginally resolved blue wing from the weaker doublet line, and are often accompanied by H_β making them unlikely to be misidentified (Baronchelli et al. 2020). In the z range of 0.7–0.9, about 29% of the systems are single-line systems, higher than the average value of 15% at all redshifts. The combination of noisier spectra and single emission line identification contributes to the ELG number drop in this redshift range.

In addition, we also compare the K -corrected absolute H -band magnitude and the $H_{\alpha\text{raw}}$ flux distributions in Figure 2 (middle and bottom). Since we do not have the mass measurements for the whole galaxy sample, we instead use the absolute H -band magnitude as a proxy for the stellar mass. Despite their comparable median and standard deviation: -21.9 ± 1.5 for pairs; -21.6 ± 1.7 for the control; the K-S test probability is 0.005 for the absolute H -band magnitude comparison, indicating intrinsically different distributions. The pair sample shows a higher fraction of luminous members at $M_H < -22$. This is a selection effect related to both the lack of enough luminous isolated ELGs at $M_H < -22$ and the bias against fainter ELG pairs, where both members are required to have at least one ELG detected at $> 3\sigma$. The $H_{\alpha\text{raw}}$ distribution also differs between the pair and control samples, with the ELG pair sample showing higher median flux: $(1.45 \pm 3.31) \times 10^{-26} \text{ erg s}^{-1} \text{ cm}^{-2}$ for pairs; $(1.31 \pm 3.57) \times 10^{-26} \text{ erg s}^{-1} \text{ cm}^{-2}$ for the control, where the comparable errors show the standard deviations. This is consistent with the SFR enhancement reported later in Section 3.

2.4. [N II] Correction

Since the WFC3 grism spectra do not resolve the [N II] $\lambda 6548 + 6583$ doublet from the H_α emission, we needed to apply a correction to the [N II]-blended $H_{\alpha\text{raw}}$. In earlier WISP studies, either a uniform average flux correction of 29% was applied (Colbert et al. 2013), or mass-dependent binned correction values ranging from 4.5%–19.5% were used (Domínguez et al. 2013). Based on high-resolution Magellan/Folded-port Infrared Echellette (FIRE) spectra of individual WISP galaxies at $z < 1.5$, flux corrections from 6.4%–39.7% were measured in Masters et al. (2014) with an average of $\sim 17.5\%$. As the [N II] correction is found to be redshift- and mass-dependent (Erb et al. 2006; Sobral et al. 2012; Masters et al. 2014), the H_α fluxes corrected with a uniform value may be underestimated for the less-massive sources and overestimated for the more massive galaxies.

In this paper, we adopted the average of two different methods to correct the [N II] from $H_{\alpha\text{raw}}$, similar to Domínguez et al. (2013) and Atek et al. (2014). We first applied the redshift- and stellar mass-dependent correction function from Faisst et al. (2018). For galaxies with no stellar mass estimates, we used an empirical conversion of $\log M_* = \kappa \times M_H + c$, where M_H is the K -corrected absolute H -band magnitude, $\kappa = (-0.4 \pm 0.1)$, and $c = (1.2 \pm 2.2)$ (Figure 3). These values are derived from the 27% WISP ELGs (2205/8192) with M_H , IRAC coverage, and SED-based mass measurements. The [N II] corrections are 9%, 16%, and 33% in the three mass bins: $\log(M_*/M_\odot) < 9$, $9 < \log(M_*/M_\odot) < 10$, and $\log(M_*/M_\odot) > 10$. Given the high

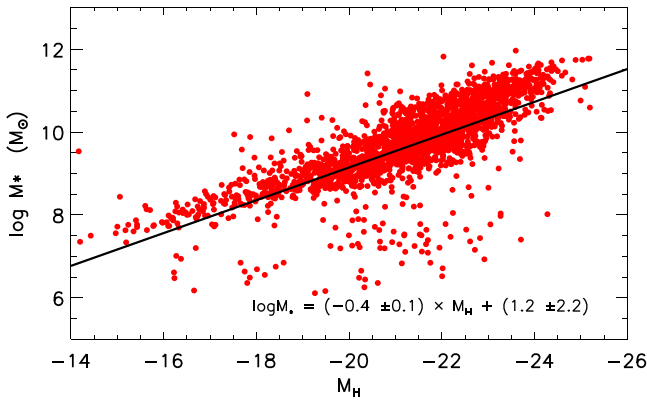


Figure 3. The distribution of the subsample of 2205 ELGs with stellar mass estimates from CIGALE (colored dots) as a function of the K -corrected absolute H -band magnitude. The straight line shows the best-fit linear correlation between the stellar mass and M_H , with the slope and interception listed in the legend. This corresponds to a directly linear proportionality between the infrared light and the stellar mass.

model dependency of the mass estimates, we also derived the $[\text{N II}]/\text{H}_\alpha$ ratio from the EW of $\text{EW}(\text{H}_{\alpha\text{raw}})$. This is based on the empirical relation from Sobral et al. (2012). The corresponding $[\text{N II}]$ contributions to the total line blend are 11%, 14%, and 21% in the three mass bins, respectively. Thus, averaged correction factors of 10%, 15%, and 27% were removed from the $\text{H}_{\alpha\text{raw}}$ flux in the corresponding mass bins.

3. Star Formation in ELG Pairs

In this section, we will focus on galaxies with SFR estimates from the H_α emission line measurements, which are the majority of the ELG sample. In 93.5% of the ELG pairs, either one (2.0%) or both (91.5%) member galaxies have an H_α detection. In comparison, given their ELG nature, 93.7% of the control group also have H_α detections.

We first perform the extinction correction for the $[\text{N II}]$ -removed H_α flux based on the $E(B - V)$ calculated from the observed Balmer decrements. Since not all Pairs in our sample have access to both H_α and H_β lines, we adopt the mean extinction values from all ELGs with $\text{H}_\alpha/\text{H}_\beta$ values in three mass bins of $\log(M_*/M_\odot) < 9$, $9 < \log(M_*/M_\odot) < 10$, $\log(M_*/M_\odot) > 10$. The average $E(B - V)$ in these bins are: [0.07, 0.06, and 0.17] mag, respectively. These values are calculated following the reddening curve of A_{H_α} from Calzetti et al. (2000), assuming an intrinsic $\text{H}_\alpha/\text{H}_\beta$ ratio of 2.86 for Case B recombination (Osterbrock 1989). Our results are consistent with the values derived in Domínguez et al. (2013) for similar WISP ELGs at $0.75 < z < 1.5$, Atek et al. (2014) for ELGs at $0.3 < z < 2.3$, and in Momcheva et al. (2013) for ELGs at $z \sim 0.8$. These extinction values are then applied to each stellar mass bin to correct for the dust attenuation.

The SFR was calculated based on the Kennicutt (1998) relation (corrected for extinction), assuming a Salpeter IMF:

$$\text{SFR}(M_\odot \text{ yr}^{-1}) = 7.9 \times 10^{-42} L_{\text{H}_\alpha}(\text{erg s}^{-1}), \quad (1)$$

where L_{H_α} is the luminosity of the $[\text{N II}]$ and dust extinction-corrected $\text{H}_{\alpha\text{raw}}$ emission line. We then divided the SFR by a factor of 1.8 to match the Chabrier IMF (e.g., Gallazzi et al. 2008). For both pair and control samples, we limit our SFR analysis to systems with H_α measurements for a more reliable SFR estimate, e.g., Hicks et al. (2002) showed clear offset

between SFR estimated from H_α and $[\text{O II}]$. This rejects 6.5% of the pair sample and 7% of the control sample, where only $[\text{O III}]$ is available. Since we rely on H_α for the SFR estimates, and base the following discussion only on the comparisons between Pairs and the control sample of isolated ELGs, the AGN contribution is ignored in the following discussion. As we will discuss later in Section 5, comparable AGN fractions are found in the pair and control samples.

We compare the distributions of extinction-corrected SFR estimates for the ELG Pairs to the control sample. Figure 4 shows the SFR versus redshift distribution, divided into two redshift bins below and above $z = 0.75$, where the two grisms overlap. For each subsample, the errors are the standard deviation from the IDL curve fit assuming the power-law function:

$$\log(\text{SFR}) = p0 + p1 \times (z), \quad (2)$$

where $p0$ and $p1$ are the intercept and slope of the power-law fit, and the input SFR is weighted by the S/N of the H_α emission line. Overall, the pair sample shows marginally elevated SFRs with respect to the isolated ELGs. Compared to the control group, the median SFRs for the subsample of wide, secure, and merging Pairs are enhanced by $(1.5 \pm 0.3)\times$, $(2.1 \pm 0.8)\times$, and $(1.6 \pm 0.4)\times$ at $z < 0.75$ and by $(1.4 \pm 0.1)\times$, $(1.5 \pm 0.4)\times$, and $(0.9 \pm 0.3)\times$ at $z > 0.75$, respectively. Across all redshifts, we find an average enhancement of $(40 \pm 20)\%$ in pairs. Table 3 summarizes the enhancement values for different subsamples of the ELG pairs.

We then consider the major Pairs in our sample (i.e., $\sim 70\%$ of our sample, based on H -band flux ratios). Compared to isolated ELGs, the median SFR for major Pairs show an average enhancement of $(2.1 \pm 0.5)\times$ and $(1.4 \pm 0.1)\times$ at low and high z , respectively. These enhancements could be further broken down into $(2.3 \pm 0.5)\times$, $(2.4 \pm 1.1)\times$, $(1.6 \pm 0.4)\times$ and $(1.5 \pm 0.1)\times$, $(1.5 \pm 0.2)\times$, $(0.9 \pm 0.3)\times$ for the $z < 0.75$ and $z > 0.75$ bins. Compared to all pairs, the major Pairs show a marginal increase in the level of the SFR enhancement, especially at $z < 0.75$ for major Pairs in the wide and secure subsamples, but not in the merging samples, which has limited statistics. Across all redshifts, the average enhancement in major Pairs is $(60 \pm 20)\%$.

Next, we only consider Pairs with $\Delta_V < 300 \text{ km s}^{-1}$, which are the systems most likely to be undergoing interactions. About 25%, 60%, and 62% of the wide, secure, and merging Pairs meet this stricter Δ_V selection. Pairs closer in physical space are more likely to be associated. The average enhancements at low and high z are $(2.1 \pm 0.5)\times$ and $(1.5 \pm 0.1)\times$, respectively. Their SFR enhancements are $(2.5 \pm 0.4)\times$, $(2.4 \pm 1.5)\times$, and $(1.6 \pm 0.3)\times$ at $z < 0.75$, and $(1.4 \pm 0.2)\times$, $(1.5 \pm 0.6)\times$, and $(0.9 \pm 0.2)\times$ at $z > 0.75$, respectively. After applying the Δ_V constraint, the enhancement at lower z becomes more significant, while at higher z the SFR enhancement remains almost the same with and without any additional selection criteria. This results in an average SFR enhancement of $(65 \pm 20)\%$.

Overall, these results are comparable to what was found in local SDSS pairs, where SFR enhancements of $1.2\times$ – $1.5\times$ were observed with a 10%–20% uncertainty at separations between 150 and 30 kpc (e.g., Patton et al. 2013), corresponding to the wide and secure Pairs in our sample. Our slightly higher enhancement in the secure Pairs may be related to the

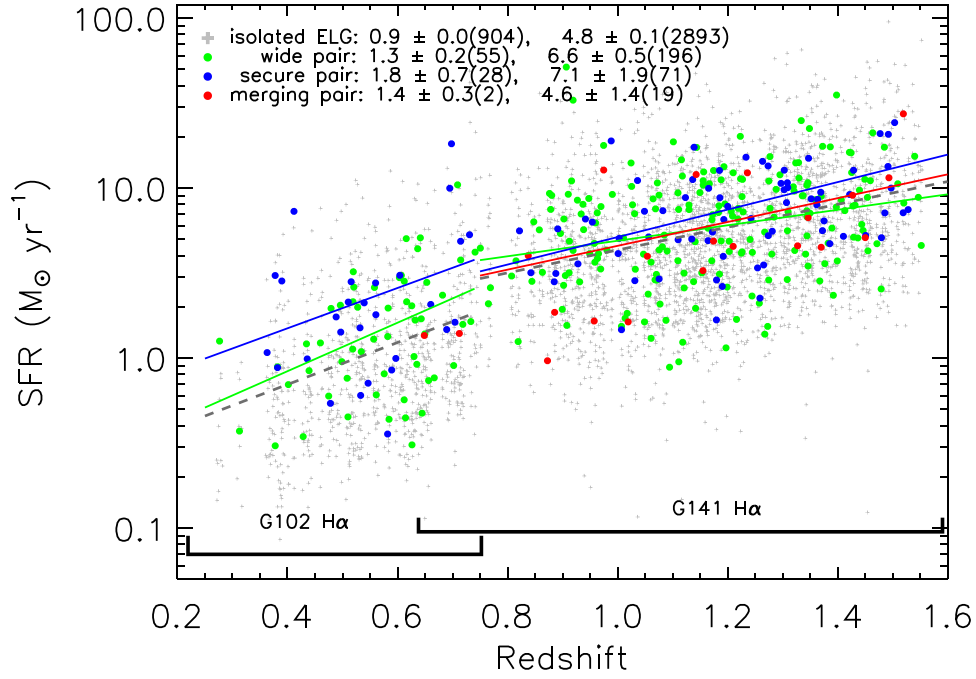


Figure 4. The redshift-SFR relation for in ELG Pairs (colored dots) and the control sample of isolated ELGs (gray crosses). SFR are derived from H_α emission line fluxes, corrected for [N II] contamination and dust extinction. The green, red, and blue dots mark the SFR in the wide, secure, and merging Pairs in our sample. The corresponding lines are the z versus $\log(\text{SFR})$ linear fit for each category, weighted by SFR uncertainties and binned in two redshift ranges ($z < 0.75$ and $z > 0.75$), corresponding to G102 and G141 coverages. In the legend, we show the median and standard deviation of the SFR in each bin, with the number of objects in the brackets for each bin. Due to small number of statistics, no fit was given for the merging Pairs at low z . Except for the merging pairs, average SFR enhancements of $1.4 \times$ – $2.1 \times$ are observed between the ELG pair subsamples and the control sample of isolated galaxies.

Table 3
SFR Enhancement in the Pair Samples

Subsamples	#	SFR Enhancement	#	SFR Enhancement
		$z < 0.75$	$z > 0.75$	
Wide	55	1.5 ± 0.3	196	1.4 ± 0.1
Secure	28	2.1 ± 0.8	71	1.5 ± 0.4
Merging	2	$(1.6 \pm 0.4)^a$	9	0.9 ± 0.3
Major pairs				
Wide	30	2.3 ± 0.5	133	1.5 ± 0.1
Secure	20	2.4 ± 1.1	49	1.5 ± 0.2
Merging	2	$(1.6 \pm 0.4)^a$	18	0.9 ± 0.3
$\Delta_V < 300 \text{ km s}^{-1}$				
Wide	20	2.5 ± 0.4	48	1.4 ± 0.2
Secure	14	2.4 ± 1.5	43	1.5 ± 0.6
Merging	1	$(1.6 \pm 0.3)^a$	12	0.9 ± 0.2
Morphology				
Disturbed	15	1.9 ± 0.5	97	1.5 ± 0.1
Compact	64	1.7 ± 0.4	164	1.3 ± 0.2

Notes. All enhancements are calculated with respect to the median SFR values for the control sample in the corresponding redshift bins.

^a Enhancement values calculated from the average SFR and their associated error.

ELG nature of this sample, when both members have to satisfy the ELG selection. The enhancement is also more significant among the lower- z pairs, especially when only considering the major or $\Delta_V < 300 \text{ km s}^{-1}$ subsamples. This is consistent with the results of Xu et al. (2012a). The much higher enhancement (2 – $3 \times$) found in SDSS for their $D_{\text{proj}} < 10 \text{ kpc}$ Pairs is not seen

here in our merging Pairs (0.9 – $1.6 \times$ enhancement), possibly related to our small number statistics. Although dust extinction is corrected in our analysis, we note that if merging Pairs suffer higher dust extinction than isolated galaxies, the average correction applied to the SFR, based on all ELGs in the mass bins, may still be significantly underestimated in merging pairs. It is worth noting that we are comparing the SFR in ELG Pairs and isolated ELGs. If quiescent galaxies were also included in the control sample, the actual enhancement is likely to be higher than what is reported here.

Next, we make the SFR comparison between normal Pairs and the Pairs with disturbed morphology. We find enhanced SFR in the 112 Pairs showing tidal tails or disturbed morphology—likely in the process of merging. At the low and high z , the disturbed Pairs show SFR enhancement of (1.9 ± 0.5) and $(1.5 \pm 0.1) \times$ over the isolated ELGs, but no more than a marginal SFR increase compared with the compact ELGs (1.1 ± 0.3 and 1.1 ± 0.1 , respectively).

We then study the SFR enhancement as a function of pair separations (Figure 5). To minimize the redshift effect, we normalize the SFR to $z = 0.75$, by adopting the average linear correlations for the pair sample in Figure 4:

$$\log(\text{SFR}) = (-0.37 \pm 0.78) + (1.16 \pm 1.32) \times z \quad (3)$$

for $z < 0.75$, and

$$\log(\text{SFR}) = (-0.04 \pm 0.14) + (0.64 \pm 0.40) \times z \quad (4)$$

for $z \geq 0.75$. In Figure 4, an insignificantly negative slope (-0.0009 ± 0.0019) is observed for the full ELG Pairs sample. After binning the data by separations (Figure 5, red crosses), the marginal increase of SFR toward smaller separation is confirmed, especially from $\sim 50 h^{-1} \text{ kpc}$: the SFR is on average 25%–35% higher at 20 – $5 h^{-1} \text{ kpc}$ than at $\sim 45 h^{-1} \text{ kpc}$, though

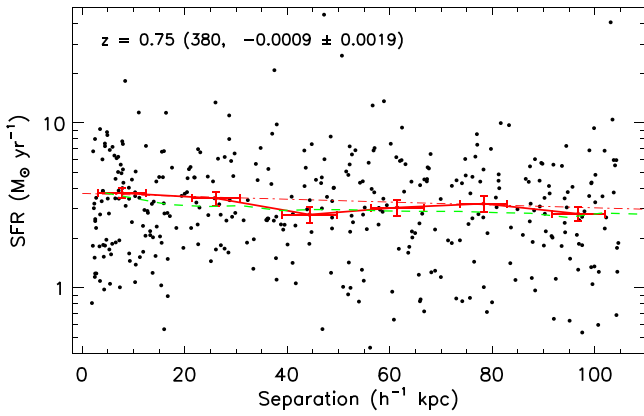


Figure 5. The average SFR in ELG Pairs as a function of pair separation, normalized to a redshift of $z = 0.75$. The number of objects and the slope are marked in the legend. The dashed-dotted line marks the linear fit between the separation and $\log(\text{SFR})$. The observed negative slope is consistent with slightly enhanced SFR toward smaller separation. The median SFRs and corresponding mean standard deviations in bins of separations are marked in red crosses. The dashed green line marks the relation for local SDSS Pairs at $z < 0.2$ (Patton et al. 2013), normalized to our data point at $\sim 100 h^{-1} \text{ kpc}$. Despite the large uncertainties, the binned SFR shows a general trend of increasing toward smaller separations, especially between ~ 50 and $5 h^{-1} \text{ kpc}$. The level of SFR enhancement in ELG Pairs is consistent with the local relation for SDSS pairs.

at a $< 1\sigma$ level. Increased SFR at low pair separation is often associated with interaction-triggered star formation, as observed in local galaxies (Figure 5, green dashed line). The SDSS relation is also plotted at $z = 0.75$ (green curve), normalized to the binned SFR at $\sim 100 h^{-1} \text{ kpc}$, for a better comparison with our sample. The amount of SFR increase is comparable: 25%–43% from ~ 45 to $5\text{--}20 h^{-1} \text{ kpc}$. Further out, SDSS sees an SFR enhancement of $\sim 10\%$ from $\sim 100\text{--}45 h^{-1} \text{ kpc}$, and the ELG Pairs also show a $\sim 10\%$ increase in the same distance range. In brief, the ELGs Pairs show a weak increase in SFR toward smaller separation, similar to what was found locally with the SDSS pairs.

4. Emission Line Ratios

Our grism spectra enable the study of emission line properties over a range of galaxy parameters including separations (pair type), redshift, line EW, and SFRs. In this section, we use spectral stacking to explore the variations of the emission line ratios in various subsamples of ELG pairs. Only galaxies with both G102 and G141 coverage are included in the following analysis. This applies to 75% of the pair sample (309 pairs) and 72% of the control sample (2934 galaxies).

We adopt a stacking procedure as detailed in Henry et al. (2013) and Domínguez et al. (2013). In brief, after masking out the emission line regions, we first subtract a model continuum for each galaxy in the rest frame. All spectra are visually inspected to make sure the subtraction is properly carried out. This is done by smoothing with a 20 pixel boxcar for the G102 (dispersion of $24.5 \text{ \AA pixel}^{-1}$) and a 10 pixel boxcar for G141 ($46.5 \text{ \AA pixel}^{-1}$). To have an equal contribution from all galaxies, we normalize each spectrum by selected emission line flux, measured from fitting a single Gaussian profile in the line region. As will be described below, H_α and [O III] fluxes are used for normalization, respectively, in the selected redshift bins for stacking. In the case of high- z sources (e.g.,

[O III]/[O II](3727 \AA) ratios, see below), where H_α falls out of the spectral coverage, [O III] flux is used for the normalization. Then, after combining the normalized spectra, we use the median value to generate the stacked spectrum. Finally, in each bin, we use the bootstrap method to resample the input spectra, estimating the errors from the rms of 500 artificial stacks.

Figure 6 shows examples of the stacked median spectra for our pair subsamples in selected bins. For comparison we also plot the stack of the control sample of isolated ELGs at the same redshift range (bottom left). We only compare the stacked spectra in the range of $0.69 < z < 1.51$, where both H_α and [O III] lines are covered. The emission line ratios of H_α to [O III] are then calculated by fitting the spectra, allowing up to three Gaussians per line, to allow multiple velocity components, to account for the possible contribution of [N II] and the weaker [O III] doublet, which is fixed at one-third of the flux of the stronger [O III] doublet. We repeat the same procedure to calculate other line ratios ([O III]/[O II], [S II]/[O II], and H_α/H_β) in different redshift ranges, and in different SFR and EW bins. Here, the mean SFR of the paired galaxies is used in the three SFR bins, and for the EW bins, we require both pair members to satisfy the requirement of being included in the stack.

Table 4 summarizes the relative line ratios from the stacked spectra in different redshift bins, with $S/N > 3$ ratios marked in boldface. The Pairs are divided into three redshift ranges, where these lines are covered: $0.69 < z_1 < 1.51$ (H_β , [O III], H_α , [S II]), $1.28 < z_2 < 1.45$ ([O II], H_α , [S II]), and $1.28 < z_3 < 2.29$ ([O II], [O III]). No ratio is recorded if the stacked spectra are missing certain lines or is too noisy ($S/N < 1$). We note that the stacked flux ratios may be inconsistent with the individual measurements, due to a combined effect of bias by the non-detection of the emission lines—other than the H_α or [O III] lines used for normalization; universal [N II] correction for the H_α flux—instead of mass-independent correction in the individual pairs, and the lack of dust-extinction correction for the stacked spectra—otherwise applied to individual spectra. Therefore, the absolute values of the stacked line ratios should be used with caution. In the following discussion, we only focus on the trends of the line ratios presented in the stacked spectra.

Various factors such as gas density, metallicity, ionization parameter, and ionizing spectral index could each influence the observed line ratios in different ways (Yan & Blanton 2012). First of all, compared to the control sample, the overall higher SFR (see Section 3) found in Pairs is reflected in their relative line ratios, which indicate that Pairs may have lower ionization levels or higher metallicities (Table 4). We notice that the H_α /[O III] ratio tends to be higher in Pairs than in the control sample, as shown in Figure 2. This would be consistent with an enhanced star formation and possibly higher metallicities, which could be related to the two times larger masses of the pair galaxies. As the SFR increases from low SFR ($1\text{--}10 M_\odot \text{ yr}^{-1}$) to high SFR ($> 10 M_\odot \text{ yr}^{-1}$), we find a significant increase in the H_α /[O III] ratio. Disturbed and merging Pairs also show marginally higher H_α /[O III] ratios, consistent with enhanced SFR in these systems. On the other hand, the low H_α /[O III] ratio in the high-EW bin is due to their noisy stacked spectra, where the [O III] line is blended in with the H_β line, yielding a higher [O III] flux with very low S/N . For the medium SFR bin, the lower ratio is real and caused by the relatively weaker H_α + [N II] line. In comparison, the H_α /[S II] ratios are generally lower in Pairs than in the control sample, suggesting an overall stronger [S II]. One possibility is shock excitation powered by tidal

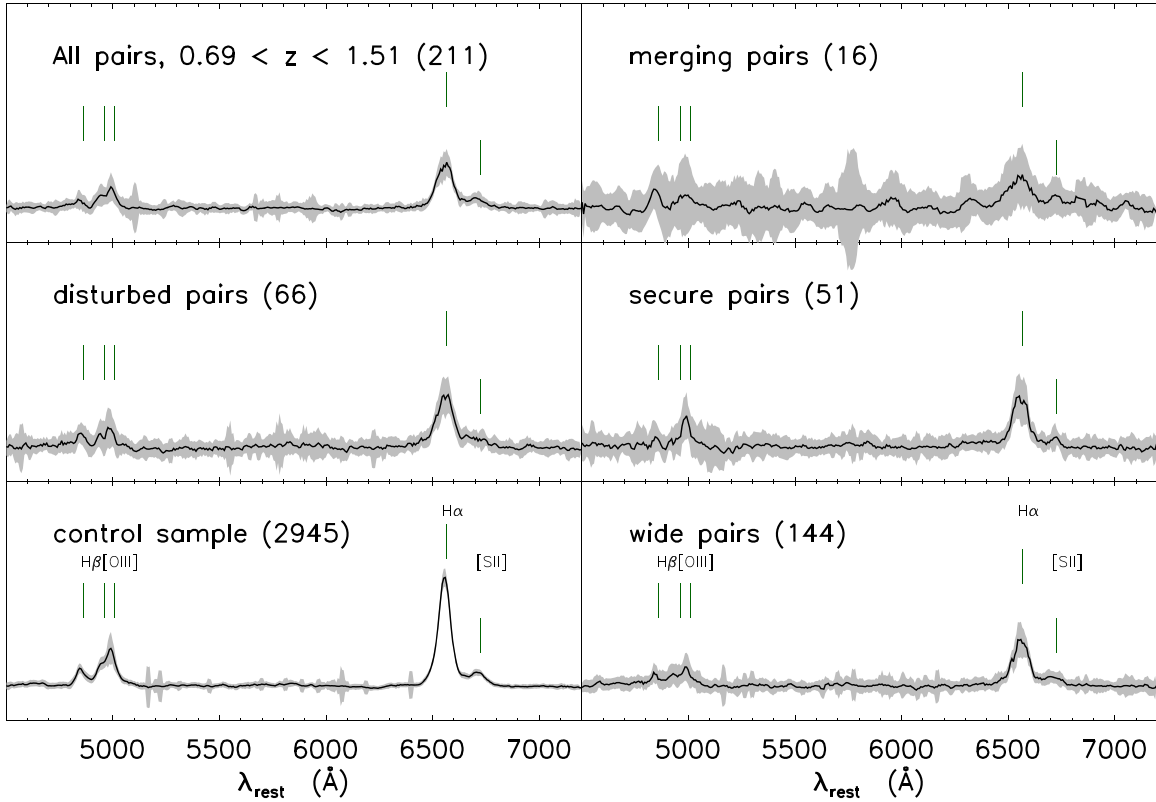


Figure 6. Stacked median spectra (continuum subtracted) for ELG Pairs in bins of pair types, with 1σ errors in gray. In brackets are the numbers of spectra included in each stack. Only Pairs with certain z range and full grism coverages are included, to ensure simultaneous H_α and $[O\text{ III}]$ coverage. The three right panels are the subsets of *all pairs* (top left panel), while the middle left panel (*disturbed*) includes all the disturbed Pairs regardless of their separation and velocity difference.

Table 4
Emission Line Flux Ratios of the Stacked Spectra

Galaxy Type	N_1	$H_\alpha^a/[O\text{ III}]$	H_α/H_β	$H_\alpha/[S\text{ II}]$	$[O\text{ III}]/H_\beta$	N_2	$H_\alpha/[O\text{ II}]$	$[S\text{ II}]/[O\text{ II}]$	N_3	$[O\text{ III}]/[O\text{ II}]$
Control sample	2945	2.18 ± 0.16	6.58 ± 0.84	5.21 ± 0.42	3.02 ± 0.49	455	4.31 ± 2.72	1.30 ± 0.97	758	3.16 ± 0.31
All pairs	211	2.55 ± 0.52	8.09 ± 2.98	4.24 ± 0.94	3.18 ± 1.24	50	3.36 ± 0.58	0.46 ± 0.12	87	2.27 ± 0.96
Disturbed	66	3.55 ± 1.20	6.41 ± 2.52	4.68 ± 1.37	1.81 ± 0.98	14	3.93 ± 2.78	0.91 ± 0.84	26	2.77 ± 1.52
Merging	16	3.54 ± 2.87	...	3.33 ± 2.02	...	3	3.18 ± 0.90	0.57 ± 0.31	8	2.44 ± 0.76
Secure	51	1.98 ± 0.59	9.89 ± 8.47	6.23 ± 3.15	4.99 ± 4.63	10	24	3.44 ± 1.97
Wide	144	2.91 ± 0.71	6.08 ± 2.09	4.73 ± 1.29	2.09 ± 0.90	37	9.09 ± 8.15	...	55	1.81 ± 0.94
EW [Å]										
>500	23	1.86 ± 0.89	3.73 ± 2.17	5.07 ± 2.06	2.01 ± 1.59	4	1.51 ± 0.04	0.03 ± 0.02	11	3.24 ± 0.82
100–500	146	3.41 ± 1.15	7.55 ± 4.08	4.31 ± 1.17	2.22 ± 1.53	33	3.62 ± 2.31	0.75 ± 0.57	39	1.77 ± 1.15
<100	8	2	17	1.52 ± 0.56
SFR ^b [$M_\odot\text{ yr}^{-1}$]										
>10	58	4.47 ± 1.54	9.29 ± 4.42	5.54 ± 1.67	2.08 ± 1.32	19	1.97 ± 0.86	0.70 ± 0.34	31	1.96 ± 1.02
1–10	153	1.48 ± 0.19	3.20 ± 0.63	3.07 ± 0.49	2.15 ± 0.40	31	4.82 ± 2.55	1.15 ± 0.73	40	6.47 ± 4.93

Notes. Given the bias against individual under-detection of multiple lines, and the mass-independent treatment of $[N\text{ II}]$ correction and the lack of dust-extinction correction, the absolute values reported in this table should be used with caution. They are listed to show the trends of the various line ratios between different subsamples. Here N_i refer to the numbers of Pairs used in each stack, which correspond to the redshift range where the relevant lines are covered: $0.69 < z_1 < 1.51$ (H_β , $[O\text{ III}]$, H_α , $[S\text{ II}]$), $1.28 < z_2 < 1.45$ ($[O\text{ II}]$, H_α , $[S\text{ II}]$), and $1.28 < z_3 < 2.29$ ($[O\text{ II}]$, $[O\text{ III}]$). Only spectra with both G102 and G141 coverages are included in the stack. Line ratios with $S/N > 3$ are highlighted in boldface.

^a Since the grism spectral resolution is not sufficient for H_α and $[N\text{ II}]$ separation, here H_α refers to the manually corrected H_α flux, with a $[N\text{ II}]$ correction of 15% applied to the $[N\text{ II}]+H_\alpha$ flux. This value is the mean correction value adopted from (Domínguez et al. 2013; Masters et al. 2014).

^b No pair with $SFR < 1 M_\odot\text{ yr}^{-1}$ falls in the selected redshift ranges listed above.

interaction in pairs, which could generate strong low-ionization (nuclear) emission line regions, i.e., LI(N)ER-like emission features (Monreal-Ibero et al. 2010; Yan & Blanton 2012; Rich et al. 2014; Belfiore et al. 2016), and cause the relatively stronger

low-ionization lines that cannot be canceled out by the SFR increase, for which H_α is the proxy.

Another possibility could be the different abundances (metallicities) or excitation mechanisms, such as diffuse

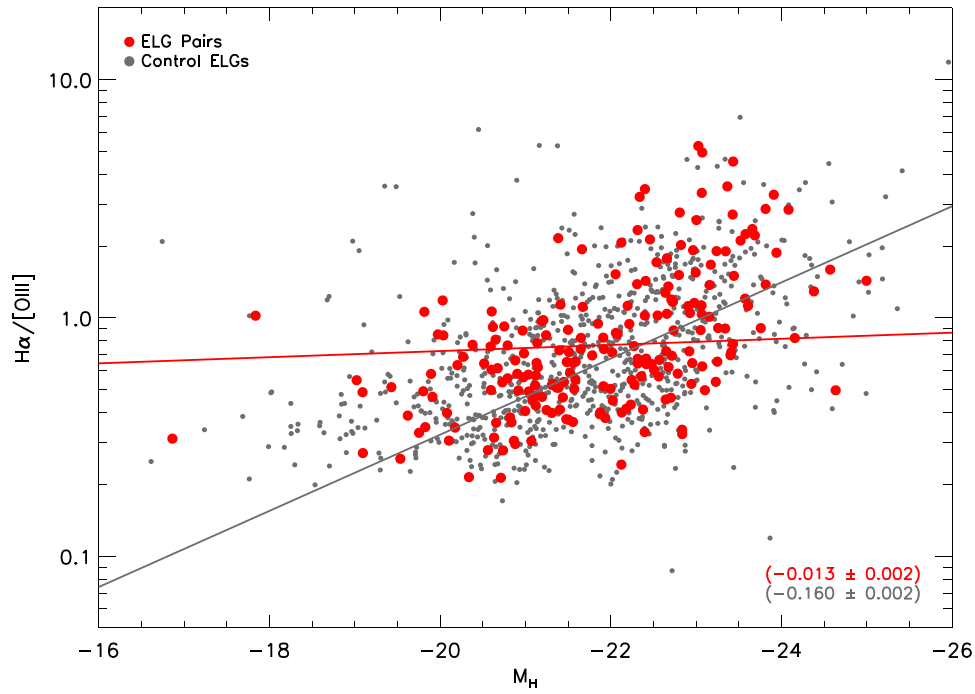


Figure 7. Distribution of the absolute H -band magnitude (M_H) vs. the H_α /[O III] line ratios for the Pairs (red) and control (gray) sample of ELGs. Only Pairs with $S/N > 3$ for both lines are plotted. We find significant correlations in both Pairs and the control sample (Spearman rank’s probability $P \ll 0.001$). The correlation coefficients with respective errors between M_H and $\log(H_\alpha/[O III])$ are given in the lower right corner.

interstellar gas or change of hardness of ionization, which can also change the H_α /[S II] ratios. To test this, we estimate the metallicities for the pair samples based on the stacked spectra using R23 (Kobulnicky & Kewley 2004). Unfortunately, given the large uncertainties, the stacked metallicities are not sensitive enough to show any significant difference between the control sample and the various pair subsamples (Table 5). The only exception is in the high SFR ($SFR > 10 M_\odot \text{ yr}^{-1}$) bin, which has a higher metallicity than the control sample. This is consistent with their relatively lower [O III]/ H_β and [O III]/[O II] ratios in Table 4, possibly related to higher masses in these high SFR objects.

To test this, we compare the H_α /[O III] line ratios with the absolute H -band magnitude, M_H , in Figure 7. The H_α /[O III] line ratios increase as the luminosity increases for both ELG Pairs and the control sample. The correlation is significant between M_H and H_α /[O III] ratios, with a Spearman rank probability $P \ll 0.001$ for both samples, consistent with a decreasing excitation temperature of H II regions with increasing galaxy mass (with M_H as a proxy). This agrees with the strong anticorrelation between [O III]/ H_α ratio and B -band luminosity found in Moustakas et al. (2006). The Pairs sample shows a flatter slope, suggesting lower excitation temperatures in low-mass galaxy Pairs compared to single galaxies; or higher excitation temperatures in more massive galaxy pairs.

The observed Balmer decrement, H_α/H_β , a measure of dust attenuation, has a large variation in different subsamples. We do not see any clear trend between the various subsamples of ELG pairs, or between the ELG pair and the control sample. The only exception is that for high SFR pairs, the Balmer decrement is also higher, indicating more dust obscuration in galaxies with the highest level of star formation. Individual measurements, after dust correction and mass-dependent [N II] removal, show that a significant fraction ($\sim 40\%$) of the Pairs that have both H_α and H_β detected ($S/N > 1$), having H_α/H_β

Table 5
Metallicity Based on the Stacked Spectra

Galaxy Type	N_3	$12+\log(O/H)$ Kobulnicky & Kewley (2004)
Control sample	758	8.82 ± 0.03
All pairs	87	$8.59^{+0.57}_{-0.32}$
Disturbed	26	$8.81^{+0.17}_{-0.12}$
Merging	8	$8.86^{+0.12}_{-0.10}$
Secure	24	$8.78^{+0.45}_{-0.18}$
Wide	55	$8.67^{+0.60}_{-0.34}$
EW [Å]		
>500	11	$7.48^{+0.19}_{-0.17}$
100–500	39	$8.92^{+0.15}_{-0.13}$
<100	17	$8.71^{+0.26}_{-0.21}$
SFR [$M_\odot \text{ yr}^{-1}$]		
>10	31	$9.05^{+0.02}_{-0.21}$
1–10	40	$8.74^{+0.47}_{-0.27}$

Note. Values derived from the stacked spectra in redshift range, $1.28 < z_3 < 2.29$, where the [O II], [O III], and H_β lines are covered.

ratio greater than 2.86. This is not surprising given the substantial amounts of reddening, commonly seen in ELGs (Ly et al. 2012; Domínguez et al. 2013). The [O III]/ H_β ratios in Pairs agree within the errors with those of the control sample. This is consistent with the result from the Baldwin-Phillips-Terlevich (BPT) diagram described in Section 5.

For $z > 1.28$, when [O II] emission lines are included, Pairs show lower H_α /[O II] and [S II]/[O II] ratios. Since the [O III]/[O II] ratio is also generally lower in pairs, this indicates an overall strong [O III] but even stronger [O II] in pairs. One possibility could be an overall lower metallicity in Pairs than in

isolated ELGs, which however was not significant within our sample, except for the high-EW bins (Table 5).

Compared to all pairs, the disturbed Pairs have marginally higher $H_{\alpha}/[\text{O III}]$ and $H_{\alpha}/[\text{S II}]$ ratios, as well as $H_{\alpha}/[\text{O II}]$, $[\text{S II}]/[\text{O II}]$, and $[\text{O III}]/[\text{O II}]$ ratios, likely due to higher $[\text{O II}]$ thus stronger low-ionization zones in such systems. For the pair types from wide to secure to merging pairs, we observe no significant trend, given their large error bars. The only exception is the increase of $H_{\alpha}/[\text{O III}]$ ratio from secure to wide pairs, which can be explained by a relatively weaker $[\text{O III}]$ in wide Pairs due to less interaction.

In short, we notice a general trend of weakly increased low-ionization emission lines in Pairs as compared to the control sample, although the degeneracy with the increased star formation, the uncertainties in line ratio and metallicity measurements, and the resolution limits make further quantitative analysis difficult at this stage.

5. ELG Pair Fraction and AGN Fraction

With this statistically significant sample up to $z \sim 1.5$, in this section we try to calculate the ELG pair fraction, and study its evolution with redshift. The biggest challenge in calculating the ELG pair fraction is the complicated completeness correction associated with the ELG nature of our sample. In this section, we will report the observed pair fractions, after applying the completeness correction based mainly on the line flux, EW, and object size (Colbert et al. 2013; Bagley et al. 2020). Due to the flux limited nature of the WISP survey, galaxies with weaker emission lines than the detection limit will be missed. As a result, an ELG with a faint companion is at greater risk of being missed than the brighter ELG pairs. We adopt the completeness corrections for the WISP ELGs (for details, see Bagley et al. 2020, Appendix A1) on an individual object-by-object basis, considering the emission line EW and *scaled flux* after adjusting for the depth differences, as well as the object size and shape, which could also affect the line detectability of the grism spectra.

Since the completeness was obtained for individual ELGs, we first estimate the average completeness in the selected redshift bins. The binned completeness is calculated by dividing the total number of ELGs by the total of the completeness (C) corrected numbers (i.e., $N_{\text{ELG}}/\sum C_i$, where C_i is the completeness for the i th object out of the N objects in the bin). The true corrected ELG pair fraction is then estimated by applying the completeness of the primary member of the pair ($C1$), the secondary member of the pair ($C2$), and the total number of ELGs in the corresponding redshift bins (Ct):

$$f = \frac{N_{\text{pair}}/(C1 \times C2)}{N_{\text{ELG}}/Ct}, \quad (5)$$

where f refers to the pair fraction.²⁰ Given the different flux values of the two members, the completeness for the secondary pair member is almost always lower than the primary pair.

We note that there are other factors, besides the line identification and detection considered above, which could also contribute to the completeness correction—border effects (i.e., missing area close to the image boundaries); decreased detector sensitivity at the blue ends of the spectra, and the correction for selection effects due to mass ratios (major versus minor),

separations, velocity offsets or galaxy types (e.g., Pairs made of ELG + quiescent galaxy). However, to convert an observed pair fraction to a merger fraction, as often reported in the literature, requires assumptions and simulations of the evolution between ELGs and other galaxy populations. A fair comparison of the ELG fraction to merger rates reported for other galaxy populations (e.g., magnitude limited, color-selected, mass-selected samples), would require knowing the normalization of all the various selection effects between the different samples, which is beyond the scope of this paper. Therefore, in the following analysis, we will only focus on the ELG population, rather than extrapolating the ELG pair fraction to the galaxy merger rate, or comparing it with other pair samples that were selected in different ways.

The observed ELG pair fraction in our spectroscopically selected pair sample shows an overall increasing trend with redshift, after the completeness correction described above (Figure 8). Except for the minor ELG pairs, we observe an increasing trend toward higher redshifts (Table 6). Unlike the full sample and major pairs, the pair fraction for minor ELG Pairs remains more or less flat over the observed redshift range, although the drastic drop at $z > 1.5$ is highly uncertain because of the small number statistics with large uncertainties. Given the fainter nature of the secondary member of the minor pairs, we are doomed to miss more minor Pairs (i.e., in which only the brighter one of the minor ELG pair is detected). This incompleteness also gets more severe at higher redshifts for the same flux limit. Therefore the fractions shown here are only lower limits for the minor ELG pairs. We then fit the ELG pair fraction with a linear slope of $f \propto (1+z)^{\alpha}$ up to $z \sim 1.6$, a region with better number statistics, as shown in Figure 2. For the full ELG pair sample, $\alpha = 0.58 \pm 0.17$, while for the major and minor pair fraction (H -band flux ratio defined, see Section 2.2.1), the linear fits show trends of $f \propto (1+z)^{0.77 \pm 0.22}$, and $f \propto (1+z)^{0.35 \pm 0.30}$, respectively. The full, major and minor ELG pair samples all have a positive α , indicating an increasing pair fraction with the redshift, although for the minor ELG pairs, the correlation is insignificant and consistent with being flat over the covered redshift range. We also note that, since some Pairs may have one quiescent member (i.e., without emission lines), the ELG pair fraction reported here is only a lower limit for the ELGs that would eventually merge with another galaxy. While on the other hand, including quiescent galaxies would also increase the number of the parent sample; thus the direction of the fraction change cannot be easily predicted. The intrinsic selection differences between the ELGs (i.e., no continuum required), and other photometry- or mass-selected samples in the literature (i.e., photometry in broad bands required), make it misleading to directly compare the various pair and merger fractions. For instance, in photometrically selected pair samples, the contamination of galaxies due to redshift uncertainties is less of an issue in the ELGs.

Finally, we estimate the AGN fractions in pairs. Based on numerical simulations, AGN activity can be triggered by the interaction of galaxies (e.g., Hopkins et al. 2006). Observational evidence of higher AGN fractions in Pairs has also been found in some studies, with a factor of 2–7 enhancement from $z \sim 0$ –1 (e.g., Ellison et al. 2011; Goulding et al. 2018). Recent work using the COSMOS and the Cosmic Assembly Near-infrared Deep Extragalactic Legacy Survey (CANDELS) pairs, however, found no significant enhancement of AGN fraction in Pairs (Shah et al. 2020). Given the ELG nature of our sample, we cannot directly compare the AGN fraction with other

²⁰ In groups of ≥ 3 members, only true Pairs qualifying the selection in Section 2 are counted, e.g., a group of three members could be counted as two Pairs or three Pairs depending on their individual physical separations.

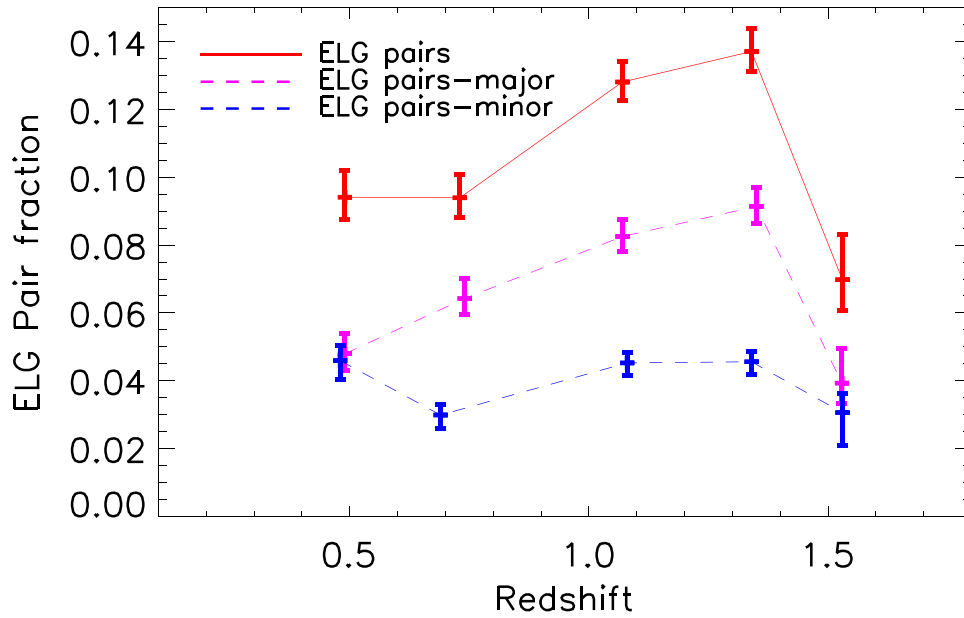


Figure 8. Completeness-corrected ELG pair fraction as a function of redshift (with Poisson errors) for the full pair sample (red), the subsamples of major (magenta) and minor (blue) ELG pairs. The drop at $z > 1.5$ regime is highly uncertain due to the small number statistics in that last bin. At $z < 1.5$, our result shows an increasing trend of the ELG pair fraction toward higher z , for both the full ELG Pairs (red solid line), and the ELG-major Pairs (magenta dashed line). The ELG-minor pair fractions (blue dashed line), on the other hand, have a flatter trend along the redshift range covered. The data used to make this plot are listed in Table 6.

Table 6
ELG Pair Fractions

Redshift Range	N_{pairs}	$\langle z \rangle$	$f_{\text{total}} (\%)$	N_{major}	$\langle z \rangle$	$f_{\text{major}} (\%)$	N_{minor}	$\langle z \rangle$	$f_{\text{minor}} (\%)$
$0.28 < z \leq 0.60$	73	0.49	$9.4^{+0.8}_{-0.7}$	40	0.48	$4.0^{+0.6}_{-0.5}$	33	0.46	$2.9^{+0.6}_{-0.4}$
$0.60 < z \leq 0.90$	82	0.73	$9.4^{+0.7}_{-0.6}$	58	0.74	$6.4^{+0.6}_{-0.5}$	24	0.69	$3.0^{+0.4}_{-0.3}$
$0.90 < z \leq 1.20$	163	1.07	$12.8^{+0.6}_{-0.6}$	108	1.07	$8.3^{+0.5}_{-0.4}$	55	1.08	$4.5^{+0.4}_{-0.3}$
$1.20 < z \leq 1.50$	172	1.34	$13.7^{+0.7}_{-0.6}$	119	1.35	$9.1^{+0.6}_{-0.5}$	53	1.34	$4.6^{+0.4}_{-0.3}$
$1.50 < z \leq 1.60^{\text{a}}$	15	1.53	$7.0^{+1.3}_{-0.9}$	8	1.52	$3.9^{+1.0}_{-0.6}$	7	1.52	$3.1^{+1.0}_{-0.6}$

Notes. $\langle z \rangle$ refers to the average z in the relevant bins. The fraction shown here has been completeness corrected following the recipes described in Section 5. The major and minor Pairs are selected by their H -band flux ratios (see Section 2).

^a $z = 1.6$ is the redshift limit below which the completeness correction, mainly based by $H_{\alpha, \text{raw}}$, is more reliable. Fitting the data up to $z = 1.6$ yields a linear correlation of $f = (0.08 \pm 0.01) \times (1 + z)^{(0.58 \pm 0.17)}$ for the whole pair sample, $f = (0.04 \pm 0.01) \times (1 + z)^{(0.77 \pm 0.22)}$ for the major pairs, and $f = (0.03 \pm 0.01) \times (1 + z)^{(0.35 \pm 0.30)}$ for the minor pairs.

studies, which usually are not limited to certain galaxy types like ELGs. We can, however, make a comparison of the AGN fraction in ELG Pairs and the control sample of isolated ELGs. Since the grism resolution does not permit H_{α} -[N II] separation, we chose the *modified-BPT* diagram using [S II]/ H_{α} and [O III]/ H_{β} (Baldwin et al. 1981; Osterbrock & Pogge 1985; Kewley et al. 2006). Here, the blended H_{α} + [N II] is corrected for with mass-dependent corrections (see Section 3). Figure 9 shows the distribution of the subsample of ELGs with all four lines detected. Unlike some of the earlier studies, we find no significant difference in the AGN fraction between Pairs and the control sample galaxies. This may be related to the ELG nature of our sample. Considering all ELGs with BPT diagnostics without any modification, the AGN fraction for the ELGs with high S/N lines (all four lines with $S/N > 3$), though suffering from small number statistics and biases, is consistent within the errors: $(33\% \pm 19\%)$ for Pairs and $(43\% \pm 10\%)$ for the control sample, respectively. We note that these AGN frequencies are likely too high because the dividing line between AGN and star-forming galaxies evolves between $z \sim 1$ and $z \sim 0$. At higher redshifts ($z > 1$), the

increased [O III]/ H_{β} ratios in star-forming galaxies would lead to their being mistaken for Seyfert galaxies if the local BPT relations were used (see for example Henry et al. 2021arXiv210700672H2021/07 The mass-metallicity relation at z 1–2 and its dependence on SFR Henry, Alaina; Rafelski, Marc; Sunnquist, Ben and 24 more). To compensate for this evolution, we test the AGN fractions based on the MEX selection (Juneau et al. 2011, 2014). Here, the stellar masses are estimated from M_H or CIGALE, if IRAC data are available (see Section 2.4). To reduce the contamination from high- z star-forming galaxies, we further apply the simple offset of 0.75 dex in stellar mass, following (Coil et al. 2015), to the Juneau et al. (2014) boundaries. The AGN fraction is $\sim 18\%$ – 19% for both Pairs and the control sample. We note that before the correction, the fraction based on MEX was also $\sim 40\%$ – 45% , similar to the local modified-BPT results. As a third test, we match our sample to the ALLWISE²¹ (Wright et al. 2010) catalog, and find an AGN fraction ($W1 - W2 > 0.8$) of

²¹ <https://irsa.ipac.caltech.edu/>

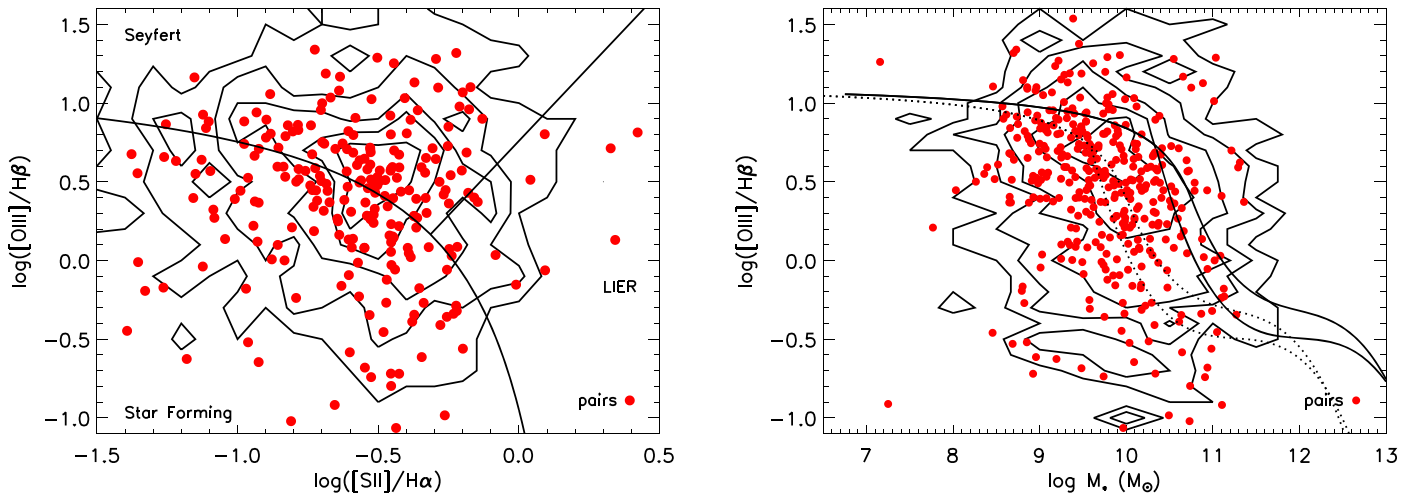


Figure 9. The distribution of the ELG Pairs (red dots) and control samples (contours) in the modified-BPT diagram (left, Baldwin et al. 1981; Kewley et al. 2006) and in the MEx diagram (right, Juneau et al. 2011; Coil et al. 2015). The dividing curves are from Kewley et al. (2006) and Juneau et al. (2014). No significant enhancement of AGN fraction is found in the pairs, with comparable fractions of $\sim 45\%$ in both samples. This fraction was also $\sim 40\%$ – 45% in the MEx diagram before the correction (dotted curves), and drops to $\sim 18\%$ – 19% after applying the offset (solid curves) from (Coil et al. 2015).

$21\% \pm 2\%$ for the control and $22 \pm 5\%$ for the pairs. Their AGN components are identified by the excess thermal emission produced by hot dust in the W2 band. Compared to AGN identification using ionized line ratios that may evolve from $z \sim 0$ to $z \sim 1$ and offset to higher values at higher redshift, using Wide-field Infrared Survey Explorer colors may yield a more reliable AGN identification at higher redshift. Although all of the above methods have a high uncertainty, the lack of enhancement in Pairs is confirmed. This is consistent with the results found in the COSMOS/CANDELS pairs, with a larger sample of more massive galaxies (Shah et al. 2020).

In summary, despite the large uncertainties in AGN fraction identification, we observe no enhancement in the AGN fraction in Pairs and the control sample of isolated ELGs.

6. Summary

By searching a total of 419 WISP fields with accurate emission line measurements, we construct a statistically significant sample of 413 ELG pair systems, including 24 merging, 109 secure, and 281 wide pairs, according to our classification scheme (Section 2). The ELG pair sample includes 47 higher-order systems with three or more members (11% of the ELG pairs). More than half ($\sim 63\%$) of our Pairs are at $z > 1$, a redshift range where spectroscopically identified Pairs were challenging to identify from ground-based observations. The WISP survey contributes the largest spectroscopically selected, unbiased galaxy pair sample at cosmic noon, countering the significant effects of cosmic variance that affects surveys limited to only small fields.

Compared to the control sample of isolated ELGs, the ELG Pairs show SFRs elevated by 40%–65% for various subsamples with different separations or velocity offsets. We observe a weak correlation between the SFR and the pair separation only at low redshift, while at higher redshift ($z > 0.75$), the correlation is flat, likely due to the large intrinsic scatter. Despite the large uncertainties, after normalization to $z = 0.75$, the ELG pair sample shows an increasing SFR at smaller pair separations, especially between ~ 50 and $5 h^{-1}$ kpc. The various line ratios based on our spectral stacking further indicate a general trend of slightly strengthened low-ionization

lines in pairs. Finally, we study the ELG pair fraction ($f \propto (1+z)^\alpha$) and find an increasing power-law index of $\alpha \sim 0.6$, though the uncertainties increase at higher redshift due to smaller number statistics, yielding different α values for the full (0.58 ± 0.17), major (0.77 ± 0.22), and minor (0.35 ± 0.30) ELG pair samples. No enhancement in the AGN fraction is found in the ELG Pairs as compared to the isolated ELGs.

The authors would like to thank the referee for helpful suggestions. Y.S.D. thanks Andrea Faisst for helpful discussions. This research is based on observations made with the NASA/ESA Hubble Space Telescope obtained from the Space Telescope Science Institute, which is operated by the Association of Universities for Research in Astronomy, Inc., under NASA contract NAS 5-26555. These observations are associated with programs 11696, 12283, 12568, 12092, 13352, 13517, and 14178. Support for this work is also partly provided by the CASSACA and Chinese National Nature Science Foundation (NSFC) grant No. 10878003. Y.S.D. acknowledges the science research grants from NSFC grants 11933003, the National Key R&D Program of China via grant No. 2017YFA0402703, and the China Manned Space Project with No. CMS-CSST-2021-A05. A.J.B. acknowledges funding from the *FirstGalaxies* Advanced Grant from the European Research Council (ERC) under the European Union Horizon 2020 research and innovation program (grant agreement No. 789056). H.A. acknowledges support from CNES.

ORCID iDs

Y. Sophia Dai (戴昱) <https://orcid.org/0000-0002-7928-416X>

Matthew M. Malkan <https://orcid.org/0000-0001-6919-1237>

Harry I. Teplitz <https://orcid.org/0000-0002-7064-5424>












Claudia Scarlata <https://orcid.org/0000-0002-9136-8876>

Anahita Alavi <https://orcid.org/0000-0002-8630-6435>

Hakim Atek <https://orcid.org/0000-0002-7570-0824>

Micaela Bagley <https://orcid.org/0000-0002-9921-9218>

Ivano Baronchelli <https://orcid.org/0000-0003-0556-2929>

Andrew Battisti  <https://orcid.org/0000-0003-4569-2285>
 Nimish P. Hathi  <https://orcid.org/0000-0001-6145-5090>
 Alaina Henry  <https://orcid.org/0000-0002-6586-4446>
 Gaoxiang Jin  <https://orcid.org/0000-0003-3087-318X>
 Crystal Martin  <https://orcid.org/0000-0001-9189-7818>
 Vihang Mehta  <https://orcid.org/0000-0001-7166-6035>
 Marc Rafelski  <https://orcid.org/0000-0002-9946-4731>
 Michael Rutkowski  <https://orcid.org/0000-0001-7016-5220>
 Hai Xu  <https://orcid.org/0000-0003-1094-5190>
 Cong K Xu  <https://orcid.org/0000-0003-2762-6057>
 Anita Zanella  <https://orcid.org/0000-0001-8600-7008>

References

- Atek, H., Kneib, J.-P., Pacifici, C., et al. 2014, *ApJ*, **789**, 96
 Atek, H., Malkan, M., McCarthy, P., et al. 2010, *ApJ*, **723**, 104
 Bagley, M. B., Scarlata, C., Mehta, V., et al. 2020, *ApJ*, **897**, 98
 Baldwin, J. A., Phillips, M. M., & Terlevich, R. 1981, *PASP*, **93**, 5
 Baronchelli, I., Scarlata, C. M., Rodighiero, G., et al. 2020, *ApJS*, **249**, 12
 Belfiore, F., Maiolino, R., Maraston, C., et al. 2016, *MNRAS*, **461**, 3111
 Bluck, A. F. L., Conselice, C. J., Buitrago, F., et al. 2012, *ApJ*, **747**, 34
 Boquien, M., Burgarella, D., Roehlly, Y., et al. 2019, *A&A*, **622**, A103
 Bournaud, F., Dekel, A., Teyssier, R., et al. 2011, *ApJL*, **741**, L33
 Bridge, C. R., Carlberg, R. G., & Sullivan, M. 2010, *ApJ*, **709**, 1067
 Bundy, K., Fukugita, M., Ellis, R. S., et al. 2009, *ApJ*, **697**, 1369
 Bustamante, S., Sparre, M., Springel, V., et al. 2018, *MNRAS*, **479**, 3241
 Calzetti, D., Armus, L., Bohlin, R. C., et al. 2000, *ApJ*, **533**, 682
 Charlot, S., & Fall, S. M. 2000, *ApJ*, **539**, 718
 Chou, R. C. Y., Bridge, C. R., & Abraham, R. G. 2012, *ApJ*, **760**, 113
 Coil, A. L., Aird, J., Reddy, N., et al. 2015, *ApJ*, **801**, 35
 Colbert, J. W., Teplitz, H., Atek, H., et al. 2013, *ApJ*, **779**, 34
 Conselice, C. J., & Arnold, J. 2009, *MNRAS*, **397**, 208
 Cox, T. J., Jonsson, P., Somerville, R. S., et al. 2008, *MNRAS*, **244**, 246
 Davies, L. J. M., Robotham, A. S. G., Driver, S. P., et al. 2015, *MNRAS*, **452**, 616
 De Propriis, R., Baldry, I. K., Bland-Hawthorn, J., et al. 2014, *MNRAS*, **444**, 2200
 de Ravel, L., Le Fèvre, O., Tresse, L., et al. 2009, *A&A*, **498**, 379
 Dekel, A., Birnboim, Y., Engel, G., et al. 2009, *Natur*, **457**, 451
 Di Matteo, P., Combes, F., Melchior, A.-L., & Semelin, B. 2007, *A&A*, **468**, 61
 Di Matteo, T., Colberg, J., Springel, V., Hernquist, L., & Sijacki, D. 2008, *ApJ*, **676**, 33
 Domínguez, A., Siana, B., Henry, A. L., et al. 2013, *ApJ*, **763**, 145
 Duncan, K., Conselice, C. J., Mundy, C., et al. 2019, *ApJ*, **876**, 110
 Ellison, S. L., Mendel, J. T., Patton, D. R., et al. 2013, *MNRAS*, **435**, 3627
 Ellison, S. L., Patton, D. R., Mendel, J. T., & Scudder, J. M. 2011, *MNRAS*, **418**, 2043
 Ellison, S. L., Patton, D. R., Simard, L., & McConnachie, A. W. 2008, *AJ*, **135**, 1877
 Erb, D. K., Shapley, A. E., Pettini, M., et al. 2006, *ApJ*, **644**, 813
 Faiss, A. L., Masters, D., Wang, Y., et al. 2018, *ApJ*, **855**, 132
 Fensch, J., Renaud, F., Bournaud, F., et al. 2017, *MNRAS*, **465**, 1934
 Gallazzi, A., Brinchmann, J., Charlot, S., et al. 2008, *MNRAS*, **383**, 1439
 Goulding, A. D., Greene, J. E., Bezanson, R., et al. 2018, *PASJ*, **70**, S37
 Henry, A., Scarlata, C., Domínguez, A., et al. 2013, *ApJL*, **776**, L27
 Hicks, E. K. S., Malkan, M. A., Teplitz, H. I., McCarthy, P. J., & Yan, L. 2002, *ApJ*, **581**, 205
 Hopkins, P. F., Croton, D., Bundy, K., et al. 2010, *ApJ*, **724**, 915
 Hopkins, P. F., Hernquist, L., Cox, T. J., et al. 2006, *ApJS*, **163**, 1
 Juneau, S., Bournaud, F., Charlot, S., et al. 2014, *ApJ*, **788**, 88
 Juneau, S., Dickinson, M., Alexander, D. M., & Salim, S. 2011, *ApJ*, **736**, 104
 Kaviraj, S., Devriendt, J., Dubois, Y., et al. 2015, *MNRAS*, **452**, 2845
 Keenan, R. C., Foucaud, S., De Propriis, R., et al. 2014, *ApJ*, **795**, 157
 Kennicutt, R. C., Jr. 1998, *ARA&A*, **36**, 189
 Kewley, L. J., Groves, B., Kauffmann, G., & Heckman, T. 2006, *MNRAS*, **372**, 961
 Kobulnicky, H. A., & Kewley, L. J. 2004, *ApJ*, **617**, 240
 Kriek, M., Shapley, A. E., Reddy, N. A., et al. 2015, *ApJS*, **218**, 15
 Law, D. R., Shapley, A. E., Checlair, J., & Steidel, C. C. 2015, *ApJ*, **808**, 160
 Law, D. R., Steidel, C. C., Shapley, A. E., et al. 2012, *ApJ*, **745**, 85
 López-Sanjuan, C., Cenarro, A. J., Varela, J., et al. 2015, *A&A*, **576**, A53
 Lotz, J. M., Jonsson, P., Cox, T. J., et al. 2011, *ApJ*, **742**, 103
 Ly, C., Malkan, M. A., Kashikawa, N., et al. 2012, *ApJL*, **747**, L16
 Man, A. W. S., Zirm, A. W., & Toft, S. 2016, *ApJ*, **830**, 89
 Mantha, K. B., McIntosh, D. H., Brennan, R., et al. 2018, *MNRAS*, **475**, 1549
 Masters, D., McCarthy, P., Siana, B., et al. 2014, *ApJ*, **785**, 153
 Mehta, V., Scarlata, C., Colbert, J. W., et al. 2015, *ApJ*, **811**, 141
 Mihos, J. C., & Hernquist, L. 1996, *ApJ*, **464**, 641
 Momcheva, I. G., Lee, J. C., Ly, C., et al. 2013, *AJ*, **145**, 47
 Monreal-Ibero, A., Arribas, S., Colina, L., et al. 2010, *A&A*, **517**, A28
 Moreno, J., Torrey, P., Ellison, S. L., et al. 2021, *MNRAS*, **503**, 3113
 Moustakas, J., Kennicutt, R. C., & Tremonti, C. A. 2006, *ApJ*, **642**, 775
 Noll, S., Burgarella, D., Giovannoli, E., et al. 2009, *A&A*, **507**, 1793
 Osterbrock, D. E., & Pogge, R. W. 1985, *ApJ*, **297**, 166
 Osterbrock, D. E. (ed.) 1989, *Astrophysics of Gaseous Nebulae and Active Galactic Nuclei* (Mill Valley, CA: Univ. Science Books)
 Patton, D. R., & Atfield, J. E. 2008, *ApJ*, **685**, 235
 Patton, D. R., Torrey, P., Ellison, S. L., Mendel, J. T., & Scudder, J. M. 2013, *MNRAS*, **433**, L59
 Qu, Y., Helly, J. C., Bower, R. G., et al. 2017, *MNRAS*, **464**, 1659
 Rich, J. A., Kewley, L. J., & Dopita, M. A. 2014, *ApJL*, **781**, L12
 Rodríguez-Gomez, V., Genel, S., Vogelsberger, M., et al. 2015, *MNRAS*, **449**, 49
 Sanders, D. B., & Mirabel, I. F. 1996, *ARA&A*, **34**, 749
 Scudder, J. M., Ellison, S. L., Momjian, E., et al. 2015, *MNRAS*, **449**, 3719
 Shah, E. A., Kartaltepe, J. S., Magagnoli, C. T., et al. 2020, *ApJ*, **904**, 107
 Snyder, G. F., Lotz, J. M., Rodríguez-Gomez, V., et al. 2017, *MNRAS*, **468**, 207
 Sobral, D., Best, P. N., Matsuda, Y., et al. 2012, *MNRAS*, **420**, 1926
 Steidel, C. C., Erb, D. K., Shapley, A. E., et al. 2010, *ApJ*, **717**, 289
 Tasca, L. A. M., Le Fèvre, O., López-Sanjuan, C., et al. 2014, *A&A*, **565**, A10
 Ventou, E., Contini, T., Bouché, N., et al. 2017, *A&A*, **608**, A9
 Violino, G., Ellison, S. L., Sargent, M., et al. 2018, *MNRAS*, **476**, 2591
 White, S. D. M., & Rees, M. J. 1978, *MNRAS*, **183**, 341
 Williams, R. J., Quadri, R. F., & Franx, M. 2011, *ApJL*, **724**, L25
 Wilson, T. J., Shapley, A. E., Sanders, R. L., et al. 2019a, *ApJ*, **874**, 18
 Wilson, T. J., Shapley, A. E., Sanders, R. L., et al. 2019b, *ApJ*, **874**, 18
 Wong, K. C., Blanton, M. R., Burles, S. M., et al. 2011, *ApJ*, **728**, 119
 Wright, E. L., Eisenhardt, P. R. M., Mainzer, A. K., et al. 2010, *AJ*, **140**, 1868
 Wuyts, S., Förster Schreiber, N. M., van der Wel, A., et al. 2011, *ApJ*, **742**, 96
 Xu, C. K., Shupe, D. L., Béthermin, M., et al. 2012a, *ApJ*, **760**, 72
 Xu, C. K., Zhao, Y., Scoville, N., et al. 2012b, *ApJ*, **747**, 85
 Yan, R., & Blanton, M. R. 2012, *ApJ*, **747**, 61
 Zanella, A., Le Floc'h, E., Harrison, C. M., et al. 2019, *MNRAS*, **489**, 2792